Technical Physics, 2022, Vol. 67, No. 9

05

Physical-mechanical properties of synthesized layers of Ti–Ni–Nb-based surface alloys, formed on the surface of TiNi alloy

© *F.A. D'yachenko, V.O. Semin, A.A. Neiman, A.R. Shugurov, L.L. Meisner, M.G. Ostapenko*

Institute of Strength Physics and Materials Science, Siberian Branch, Russian Academy of Sciences,
634055 Tomsk, Russia
e-mail: dfa@ispms.ru

Received March 14, 2022
Revised May 17, 2022
Accepted May 18, 2022

The physical-mechanical properties (microhardness, Young's modulus, plasticity characteristic, shape recovery ratio) of the synthesized layers of Ti–Ni–Nb-based surface alloys of $\sim 2\,\mu$m thickness, formed on the surface of TiNi alloy by the additive thin-film electron beam method were investigated by the instrumented indentation. It was found that the change in physical-mechanical properties in the synthesized surface alloys based on Ti–Ni–Nb is due to their layered structure. In particular, it is due to the thickness of the sublayers, their phase composition, and the structural states of the phases (nanocrystalline and amorphous). It was established that high strength and elastic-plastic parameters of the outer layer and a monotonic change in the physical-mechanical properties from the surface to TiNi substrate are provided in the surface Ti–Ni–Nb alloy with a lower volume fraction of the amorphous phase in the synthesized layers. It was found that the multilayer structure of the surface Ti–Ni–Nb alloy and the monotonically change in the physical-mechanical properties to the substrate ensure high mechanical compatibility of the synthesized layers of surface alloys with the TiNi substrate.

Keywords: nickel titanium alloy, additive thin-film electron-beam synthesis, surface alloy, structure, physical-mechanical properties.

DOI: 10.21883/TP.2022.09.54680.52-22

Introduction

The use of TiNi-based alloys with shape memory effects and superelasticity as materials for medicine is due to their ability to reversibly return a significant predetermined deformation (up to 12%) with a change in temperature and magnitude of applied external mechanical stresses [1,2]. The main limitations for including these alloys in the group of biocompatible metallic materials are:

1) chemical composition (high concentration of toxic Ni^+ ions and accordingly, their accumulation in adjacent tissues [3,4]);

2) insufficient level of radiopacity of miniature products based on these alloys [5].

Metal coatings of submicron thickness are used to functionalize the surface of metallic materials in order to increase their biocompatibility, corrosion resistance and radiopacity [6]. However, the main disadvantages of the formed coatings on the surface of TiNi-alloys are:

1) the presence of texture in crystalline coatings, which reduces their strength;

2) weak adhesive strength of coatings;

3) their thermomechanical incompatibility with the TiNi substrate.

These factors can lead to delamination of coatings from TiNi alloy substrates during operation of miniature medical products [7].

Recent studies [8–11] show that these problems can be overcome by using an additive thin-film electron-beam method for the synthesis of surface alloys (SA). The essence of this method, described in detail in [9–11], consists in repeated alternation of operations of deposition of a dopant film of a given composition and a certain thickness and subsequent liquid-phase mixing of the film and substrate components using a pulsed low-energy high-current electron beam (LEHCEB) of microsecond duration. In order to reduce the Ni concentration near the surface, increase the corrosion properties of TiNi alloys and the radiopacity of products from these alloys, the electron beam method was applied to the synthesis of three- and four-component SA based on Ti–Ni–Ta [9], Ti–Ni–Ta–Si [10] and Ti–Ni–Nb [11].

This paper is a continuation of a series of studies [9–11] aimed at creating on the surface of miniature medical products made of TiNi alloy thin ($\sim 1-2\,\mu$m thick) barrier layers of SA based on Ti with a low concentration of Ni on the surface and high physical and mechanical properties. The choice of Ta and Nb as alloying elements in the synthesized SA layers allows the surface of miniature products for medicine to function (to increase their corrosion resistance [12,13] and radiopacity [14,15]).

Earlier, in studies of the structure and physical and mechanical properties [9,10], it was shown that the synthesized multicomponent SA based on Ti–Ni–Ta [9] and Ti–Ni–Ta–Si [10] have high strength and elastic-plastic characteristics (microhardness, modulus of elasticity, plasticity, shape recovery ratio) and close mechanical compatibility of the synthesized layers to the TiNi substrate. In particular, in [9] a detailed analysis of the relationship between the structure and physical and mechanical properties in a multilayer SA based on Ti−Ni−Ta is given. It has been established that a monotonic change in physical and mechanical properties from high-strength layers of a surface Ti−Ni−Ta alloy (microhardness $H_{OP} \approx 8$ GPa, modulus of elasticity $E_{OP} \approx 105$ GPa) to the TiNi substrate ($H_{OP} \approx 3.5$ GPa, $E_{OP} \approx 55$ GPa) is carried out due to the formation of similar thicknesses (~ 300 nm) composite nanocrystalline sublayers in the transition Ti−Ni−Ta zone. In a monolayer SA based on Ti−Ni−Ta−Si [10], in which to a depth of up to $\sim 1.5\,\mu$m a layer with a completely amorphous structure was formed, the presence of nanocomposite and eutectic sublayers (up to ~ 300 nm thick) led to a monotonic change in the physical and mechanical properties from amorphous SA with high microhardness ($H_{OP} \approx 8.3$, GPa) and elastic modulus ($E_{OP} \approx 116$ GPa) to the TiNi substrate. It is important to note that the presence of SA based on Ti−Ni−Ta−Si led to an increase in the corrosion resistance of the TiNi alloy [10].

In the paper [11], multilayer SAs based on Ti−Ni−Nb were synthesized using $Ti_{85}Nb_{15}$ doping films and $Ti_{70}Nb_{30}$ (at.%). On these SA, the surface morphology and topography were studied by scanning electron microscopy and structural-phase studies were performed using transmission electron microscopy and X-ray diffraction analysis. With the help of instrumented indentation, on the example of a synthesized SA using a $Ti_{70}Nb_{30}$ alloying film, the results on physical and mechanical properties are briefly presented. Nevertheless, a detailed analysis of these properties with a comparison of the phase-structural data of individual sublayers for a given SA in [11] remains behind the scenes. In addition, data on the change in the physical and mechanical properties of the synthesized SA using a $Ti_{85}Nb_{15}$ dopant film are not given in [11]. There is no information about comparing the properties of SA relative to each other. An important issue is the effect of the Nb concentration in the doping film during SA synthesis on the physical and mechanical properties.

Thus, the purpose of this paper is to establish the patterns of changes in the physical and mechanical properties of SA based on Ti−Ni−Nb, which differ in structure and composition. To study the influence of the thickness of the sublayers, phase compositions, as well as the ratio of the volume fractions of nanocrystalline and amorphous phases in the sublayers on the strength and elastic-plastic parameters of SA and their mechanical compatibility with the TiNi substrate. It can be expected that a change in the Nb concentration in the doping film affects not only the structure, composition, and chemical composition of the SA themselves, but also the physical and mechanical properties in the synthesized layers of the system [surface Ti−Ni−Nb alloy/TiNi substrate].

1. Material, processing and research methods

Plane-parallel samples with dimensions of $10 \times 10 \times 1$ mm made of TiNi grade TN-1 (MATEK-SPF, Russia) cut from rolled sheet were used for research. The chemical composition of the alloy: Ti−55.75 Ni−0.035 O−0.02 C−0.003 N−0.001 H (wt.%); temperature of the beginning of the reverse martensitic transformation $A_S = 308$ K. Before SA synthesis, the sample surfaces were subjected to chemical etching (in a solution of acids $HNO_3 + HF$, 3 : 1 (vol.%)), mechanical grinding and electrolytic polishing ($CH_3COOH + HClO_4$, 3 : 1 (vol.%)) and washing in an ultrasonic bath with distilled water.

SA formation on the TiNi substrate was carried out in a single vacuum cycle on a modified automated setup RITM-SP (OOO Microsplav, Russia) [16]. SA prepared on the basis of systems:

1) [$Ti_{85}Nb_{15}$ film, thickness 100 nm/TiNi substrate];
2) [$Ti_{70}Nb_{30}$ film, thickness 100 nm/TiNi substrate].

A Ti−Nb film with a thickness of ~ 100 nm was deposited on the surface of a TiNi substrate by the magnetron method, simultaneously from two magnetrons, by sputtering single-component targets from pure elements Ti (99.95 wt.%) and Nb (99.95 wt.%) (Girmet, Russia). The compositions of the $Ti_{85}Nb_{15}$ and $Ti_{70}Nb_{30}$ films were controlled by energy dispersive spectroscopy (EDS) (INCA Oxford Instruments, Great Britain) on a scanning electron microscope (SEM) LEO EVO 50 (Zeiss, Germany) Center for Collective Use NANOTECH ISPMS SB RAS (Russia, Tomsk) at an accelerating voltage $U = 10$ kV. According to the measurements, the compositions of the films corresponded to the calculated ($Ti_{85/70}Nb_{15/30}$) with an accuracy of $\leq \pm 5$ at.%. The films practically did not contain carbon, the oxygen concentration in them did not exceed a few at.%. Liquid-phase mixing was performed using LEHCEB at beam energy density $E_s = 1.7$ J/cm^2 and number of pulses $n = 10$. The operations of thin film deposition and its pulsed electron-beam liquid-phase mixing with the substrate were carried out in a single vacuum cycle. The number of synthesis cycles N was repeated 10 times without removing the substrates from the working chamber of the setup. Thus, the expected effective SA thickness was $\sim 1\,\mu$m. The temperature of the TiNi substrate did not exceed 473 K by the end of the synthesis. A more detailed description of the method for synthesizing SA based on Ti−Ni−Nb is given in [11].

Electron microscopy studies using bright and dark fields, micro- and nanodiffraction analysis were performed on a transmission electron microscope (TEM) JEM-2100 (JEOL, Japan) at the Center for Collective Use NANOTECH (Russia, Tomsk) at an accelerating voltage of 200 kV. The size of the electron probe in micro- and nanodiffraction modes was ~ 200 and ~ 12 nm, respectively. Foils for TEM studies were prepared on an EM 09100IS ion etching unit (JEOL, Japan) in the „cross-section“geometry.

The strength and elastic-plastic parameters of SA were determined by the method of instrumented indentation on the NanoTest facility (Micro Materials Ltd, Great Britain) at ISPMS SB RAS (Russia, Tomsk) equipped with a Berkovich tip (3-faced diamond pyramid, half angle at the apex $\theta_B = 65.3^\circ$). The maximum load $P_{\max}$ was applied from 5 to 300 mN (11 loads). The test load profile is trapezoidal. The holding time at $P_{\max}$ was 5 s. Duration of one „loading/unloading"cycle $t = 20$ s, indentation step ~ 1 nm. The set of experimental data array for each load corresponded to ten tests, followed by statistical averaging. For each type of SA, 6 samples were subjected to testing.

According to the $P-h$ „loading/unloading" diagrams, the strength and elastic-plastic parameters were determined depending on the maximum indentation depth $h_{\max}$. The microhardness H_{OP} and the modulus of elasticity E_{OP} were calculated by the method of Oliver–Pharr [17].

The plasticity parameter δ_h, which characterizes the tendency of a material to irreversibly deform under a load P, was evaluated by the method described in [18]:

$$\delta_h = \frac{h_r}{h_{\max}} \cdot 100\%,$$

where h_r — the depth of the impression formed after unloading; $h_{\max}$ — maximum penetration depth of the tip.

The η parameter characterizing the degree of shape recovery ratio of imprint was calculated by the method described in [19]:

$$\eta = \frac{h_{\max} - h_r}{h_{\max}} \cdot 100\%.$$

2. Results and discussion

2.1. Structure of surface alloys based on Ti–Ni–Nb

According to the TEM results, earlier studies [11] showed that surface Ti–Ni–Nb alloys synthesized on a TiNi substrate have a multilayer amorphous-nanocomposite structure from a mixture of nanocrystalline, amorphous and nanocomposite phases. The synthesized layers differ in chemical and phase compositions, average grain size and grain orientation. Based on the data on the analysis of the structure of the synthesized layers, described in [11], Fig. 1 shows schematic illustrations of the multilayer structure and the main characteristics of the structures of the synthesized layers of both the SA themselves and the sublayers of the transition Ti–Ni–Nb-zones to the TiNi substrate. In these schemes, the bright-field electron microscopic images obtained in the cross section are shown as inserts, the sublayers are numbered with Roman numerals, and the thicknesses of the sublayers are marked with arrows. The scales of the original bright-field electron microscope images and the sizes of all structural elements are indicated and given in the paper [11]. The phase composition of surface Ti–Ni–Nb-alloys was previously established by X-ray diffraction and electron microscopy methods in [11].

Separation of layers in the system [surface Ti–Ni–Nb-alloy/TiNi substrate] into surface Ti–Ni–Nb-alloy and transition Ti–Ni–Nb-zone is justified by the authors on the basis of the elemental composition data along the cross section, obtained using the energy dispersive microanalysis method (TEM/EDS microanalysis). According to the results of the paper [11], the surface Ti–Ni–Nb-alloy (in this paper denoted as [TiNi–Nb_{15}]SA and [TiNi–Nb_{30}]SA) includes synthesized layers located at a depth of up to $\sim 2\,\mu$m, in which the total concentration of the alloying element is (Nb) is at least ~ 5 at.%. The transition Ti–Ni–Nb-zone is formed by a sublayer at a depth of ~ 2 to $\sim 2.4\,\mu$m, where the Nb concentration monotonically decreases in depth from ~ 5 at.% to zero.

2.1.1. The structure of the synthesized layers of the system [[TiNi–Nb_{15}]SA/TiNi-substrate]

In TiNi-samples after the formation of a surface Ti–Ni–Nb-alloy using a $Ti_{85}Nb_{15}$ alloying film, a synthesized layer including the [TiNi–Nb_{15}]SA and the Ti–Ni–Nb transition zone have a multilayer amorphous-nanocomposite structure (Fig. 1, *a*). On the basis of the conducted electron microscopic studies and TEM/EDS-microanalysis in [11] it was established that the first layer and two sublayers located behind it are the [TiNi– Nb_{15}]SA. Under the [TiNi–Nb_{15}]SA there is one eutectic sublayer, which represents the Ti–Ni–Nb transition zone.

Nanocomposite layer I with a thickness of ~ 700 nm, consists of a mixture of nanocrystalline phases of binary and ternary compositions (orthorhombic α'' (Ti, Nb) martensite, hexagonal phase Ni_6Nb_7 and fcc phases (γNi, Ti, Nb)). Nanocrystals of these phases are evenly distributed with regions with quasi-crystalline and amorphous structures. The nanocomposite structure of layer I, which is an amorphous matrix with „interspersed" nanocrystals, according to [20], can also be characterized as „amorphous-nanocrystalline composite".

Under layer I, at a depth from the surface between ~ 700 nm and $\sim 1.5\,\mu$m, there is amorphous sublayer II containing a small amount of crystalline nanoparticles of the Ti_2Ni and nanopores up to ~ 20 nm. Below amorphous sublayer II at a depth of $\sim 1.5\,\mu$m, there is nanocomposite sublayer III with a thickness of ~ 500 nm, which consists of a mixture of nanocrystalline phases (α'' (Ti, Nb), B2(TiNi), Ti_2Ni) and the amorphous phase. In this sublayer, the volume fraction of the amorphous phase is less than in sublayer II. Below sublayer III in the transition zone there is eutectic sublayer IV of thickness ~ 600 nm, which has the phase composition B2(TiNi) + Ti_2Ni. At a depth of more than $\sim 2.6\,\mu$m, the structure of the TiNi sample after synthesis of [TiNi–Nb_{15}]SA is close to the B2(TiNi) structure for the initial TiNi substrate without irradiation and doping.

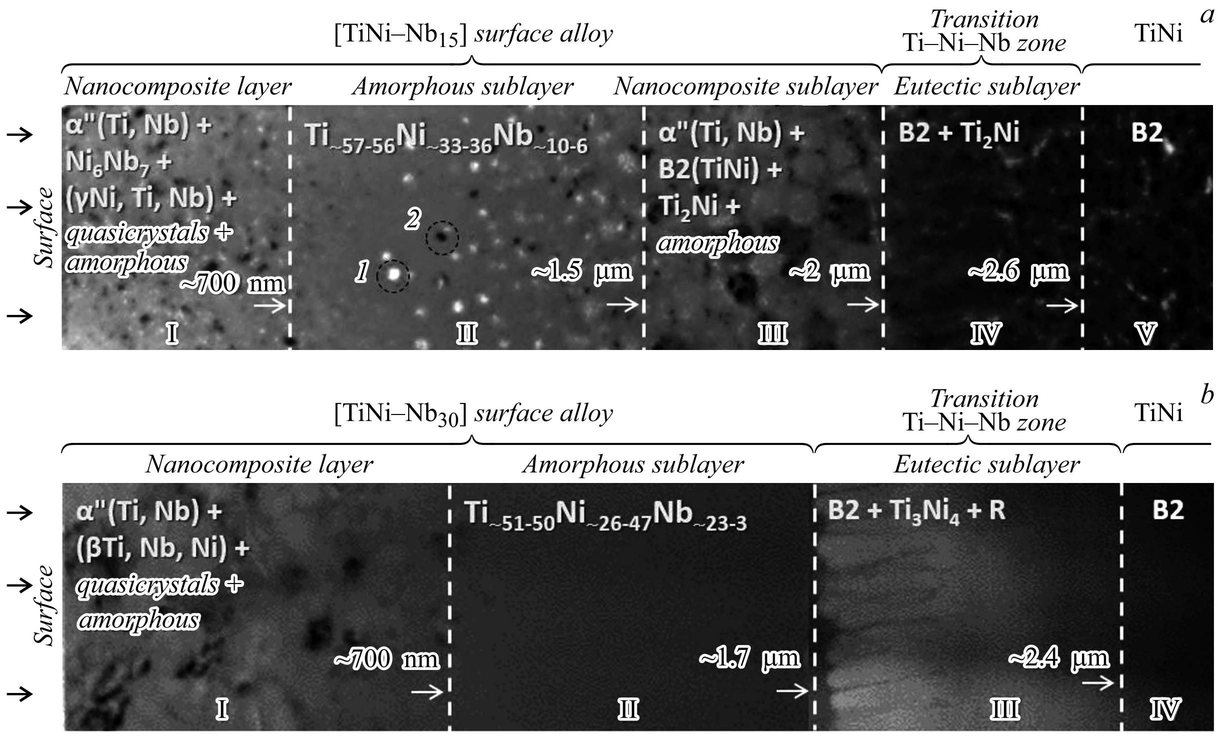

Figure 1. Schemes of the multilayer structure of the [[TiNi$-$Nb$_{15}$]SA/TiNi substrate] system (*a*) (in sublayer II: *1* — nanopore; *2* — nanocrystals of the Ti$_2$Ni phase) and [[TiNi$-$Nb$_{30}$]SA/TiNi substrate] system (*b*) built on the basis of separately obtained bright-field electron microscope images.

2.1.2. The structure of the synthesized layers of the system [[TiNi$-$Nb$_{30}$]SA/TiNi-substrate]

In TiNi-samples after the formation of a surface Ti$-$Ni$-$Nb-alloy using a Ti$_{70}$Nb$_{30}$ alloying film, a synthesized layer including [TiNi$-$Nb$_{30}$]SA and Ti$-$Ni$-$Nb transition zone, also has a multilayer amorphous nanocomposite structure [11]. However, in comparison with the three-layer [TiNi$-$Nb$_{15}$]SA (Fig. 1,*a*), the structure of [TiNi$-$Nb$_{30}$]SA consists of two layers (Fig. 1,*b*). Under the [TiNi$-$Nb$_{30}$]SA there is one eutectic sublayer, which represents the Ti$-$Ni$-$Nb transition zone.

Nanocomposite layer I with a thickness of ~ 700 nm consists of a mixture of nanophases of binary and ternary compositions (orthorhombic α'' (Ti, Nb) martensite and bcc phase (βTi, Nb, Ni)). Nanocrystalline and quasicrystalline phases are evenly distributed in the amorphous matrix of this layer. According to [11], the volume fraction occupied by the amorphous phase in this layer is greater than the volume fraction of the amorphous phase in nanocomposite layer I in [TiNi$-$Nb$_{15}$]SA. Under layer I, at a depth between ~ 700 nm and $\sim 1.7\,\mu$m, completely amorphous sublayer II free of inclusions and nanopores was formed. The transitional Ti$-$Ni$-$Nb-zone (sublayer III) ~ 700 nm thick, located at a depth of more than $\sim 1.7\,\mu$m, is characterized by a eutectic structure and phase composition B2(TiNi)+Ti$_3$Ni$_4$+R(TiNi). At a depth of more than $\sim 2.4\,\mu$m, the structure of the TiNi sample after synthesis of [TiNi$-$Nb$_{30}$]SA is close to the B2(TiNi) structure for the initial TiNi substrate without irradiation and doping.

Thus, on the basis of the above data on the structure of SA synthesized based on Ti$-$Ni$-$Nb, it was found that the change in the concentration of the doping element (Nb) when using Ti$_{85}$Nb$_{15}$ and Ti$_{70}$Nb$_{30}$ during SA synthesis, affects the phase composition, thickness and number of layers. First, with a decrease in the amount of Nb, an additional nanocomposite sublayer is formed in the three-layer [TiNi$-$Nb$_{15}$]SA (Fig. 1,*a*), in difference from the two-layer [TiNi$-$Nb$_{30}$]SA (Fig. 1,*b*), for which completely amorphous sublayer II is followed by eutectic sublayer III. Second, a decrease in the Nb concentration in the film during SA synthesis leads to a decrease in the volume fraction of the amorphous phase in the synthesized layers.

2.2. Physical-mechanical properties of surface alloys based on Ti$-$Ni$-$Nb

Let us consider how the presented features of the structure of the synthesized SA based on Ti$-$Ni$-$Nb will be reflected in the regularities of changes in the physical and mechanical properties of the synthesized layers.

For a precision study of the physical and mechanical properties of the system [surface Ti$-$Ni$-$Nb alloy/TiNi substrate], the loading conditions on the indenter from 5 to 300 mN were experimentally selected as follows. In the range of minimum loads from 5 to 20 mN, at the maximum

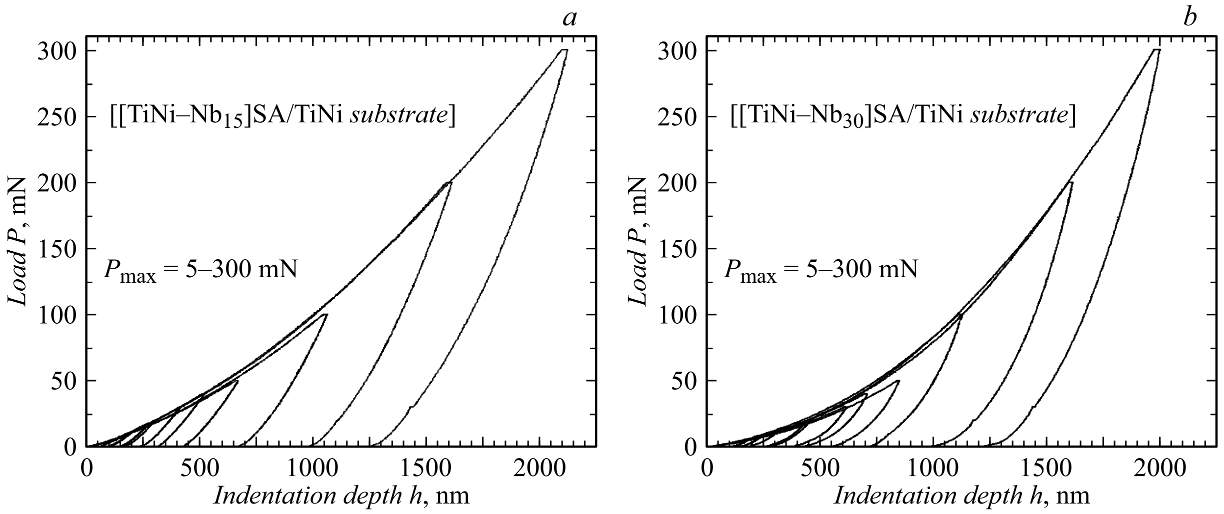

Figure 2. Diagrams $P-h$ of „loading/unloading" during indentation of the system [[TiNi–Nb]$_{15}$]SA/TiNi substrate] (a) and the system [[TiNi–Nb$_{30}$]SA/TiNi substrate] (b) with a stepwise increase in load $P_{\max}$ by the indenter from 5 to 300 mN.

penetration depth of the indenter $h_{\max}$ not exceeding ~ 500 nm, the physical and mechanical properties of the synthesized [TiNi– Nb$_{15}$]SA and [TiNi–Nb$_{30}$]SA were defined. The loading range from ~ 25 to ~ 200 mN, in turn, characterizes the integral properties of the synthesized layers for both [TiNi–Nb$_{15}$]SA and [TiNi–Nb$_{30}$]SA (at depths from ~ 500 nm to $\sim 2\,\mu$m) and for sublayers of the transition Ti–Ni–Nb-zones (at depths from ~ 2 to $\sim 2.5\,\mu$m). In the loading range from ~ 200 to ~ 300 mN, the influence of the electron-beam method of SA synthesis on the volumetric physical and mechanical properties of the TiNi substrate at a depth of more than $\sim 2.5\,\mu$m is estimated.

Fig. 2 shows „loading/unloading" diagrams $P-h$ during indentation of [TiNi–Nb$_{15}$]SA and [TiNi– Nb$_{30}$]SA with a stepwise increase in the load $P_{\max}$ on the indenter from 5 to 300 mN. Fig. 3 shows schematic illustrations of the multilayer structure and „loading-unloading" diagrams $P-h$ when indenting the system [[TiNi–Nb$_{15}$]SA/TiNi-substrate] in different loading ranges. Fig. 4 shows dependences of microhardness H_{OP}, elasticity modulus E_{OP}, plasticity parameter δ_h and degree of indentation recovery η on the maximum immersion depth of the tip $h_{\max}$ corresponding to different sublayers, as shown in the diagram in Fig. 3. Similarly, for the [[TiNi–Nb$_{30}$]SA/TiNi-substrate system, Fig. 5 shows schematic illustrations of the multilayer structure and $P-h$ diagrams; Fig. 6 shows the dependences of the change in strength and elastic-plastic parameters on the maximum tip immersion depth $h_{\max}$.

2.2.1. Physical-mechanical properties of the synthesized layers of the system [[TiNi–Nb$_{15}$]SA/TiNi-substrate]

Fig. 3 shows the schemes of the layered structure and „loading-unloading" diagrams $P-h$ when indenting the system [[TiNi–Nb$_{15}$]SA/ TiNi-substrate] in different loading ranges. As can be seen from Fig. 3, the entire loading range (Fig. 2, a) can be divided into two parts:

1) from 5 to 40 mN (Fig. 3, b), which corresponds to the maximum immersion depth of the tip $h_{\max}$ from ~ 120 to ~ 570 nm;

2) from 50 to 300 mN (Fig. 3, c), which corresponds to the immersion depth $h_{\max}$ from ~ 650 nm to $\sim 2.1\,\mu$m.

So, within each range, the process of deformation accumulation develops according to a single parabolic dependence with an increase in the load on the indenter. This result is confirmed by the constructed analytical dependences $P(h)$. In turn, this means that the physical and mechanical properties of the synthesized layers, which provide the main contribution to the mechanical response of the sample within each loading range, are uniform.

The results of studies of strength and elastic-plastic parameters characterizing changes in physical and mechanical properties showed (Fig. 4) that in a nanocomposite layer I at a depth of ~ 120 to ~ 700 nm, the values of the parameters change in a gradient. Microhardness H_{OP} decreases linearly from ~ 9 to ~ 5 GPa, elastic modulus E_{OP} decreases linearly from ~ 122 to ~ 77 GPa, plasticity parameter δ_h increases monotonically from ~ 45 to $\sim 63\%$, the shape recovery ratio η decreases linearly from ~ 55 to $\sim 38\%$ (Fig. 4, curves *1–4*). From a comparison of data on the structure (Fig. 1, a) and physical and mechanical properties (Fig. 4) for layer I, it follows that high strength (H_{OP}, E_{OP}) and low plastic (δ_h) properties are due to the nanocomposite structure. The high degree of recovery of the indenter imprint in this layer ($\eta \approx 55\%$) is associated with the mechanisms of elastic recovery (due to the high modulus of elasticity ($E_{OP} \approx 122$ GPa) characteristic of materials with an amorphous structure [21]).

In amorphous sublayer II and in nanocomposite sublayer III with a mixed amorphous-nanocrystalline structure,

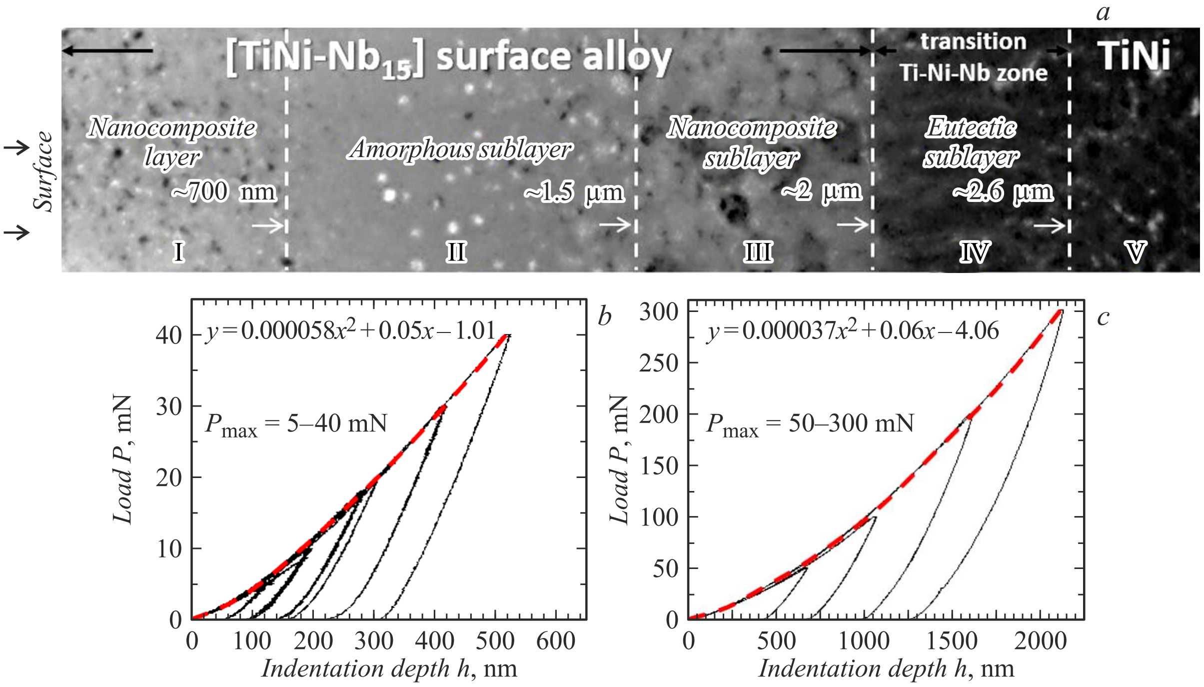

Figure 3. Scheme of the multilayer structure of the [[TiNi$-$Nb$_{15}$]SA/TiNi substrate] system with the indication of the main structural-phase states in the synthesized layers (a) and „loading/unloading" diagrams $P-h$ when indenting the system [[TiNi$-$Nb$_{15}$]SA/TiNi substrate] in the loading ranges $P_{\max}$ on the indenter 5$-$40 mN (b) and 50$-$300 mN (c).

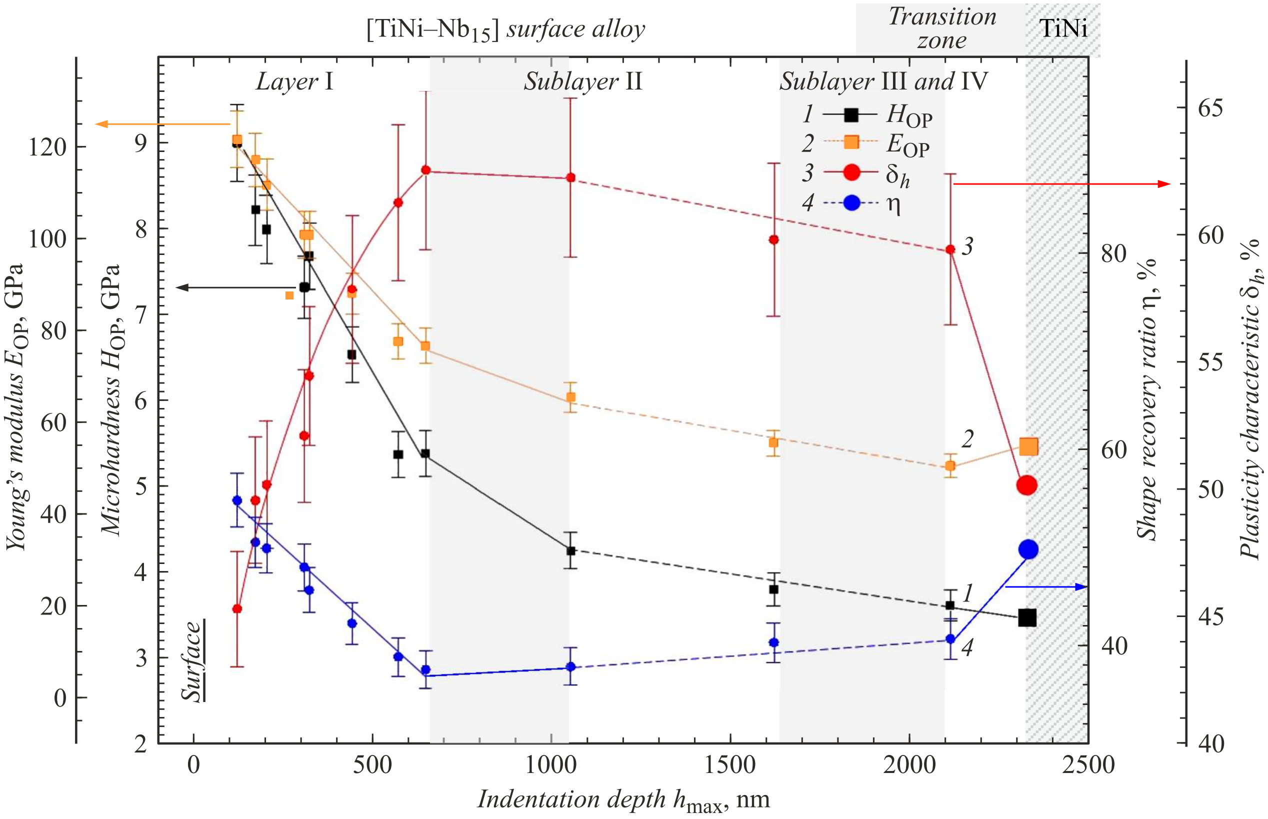

Figure 4. Dependences of microhardness H_{OP} (*1*), elasticity modulus E_{OP} (*2*), plasticity parameter δ_h (*3*) and the shape recovery ratio η (*4*) on the maximum penetration depth of the indenter $h_{\max}$ when indenting the system [[TiNi$-$Nb$_{15}$]SA/TiNi substrate] (larger symbols denote the properties for the initial TiNi sample without irradiation and doping at a depth of more than $\sim 2\,\mu$m).

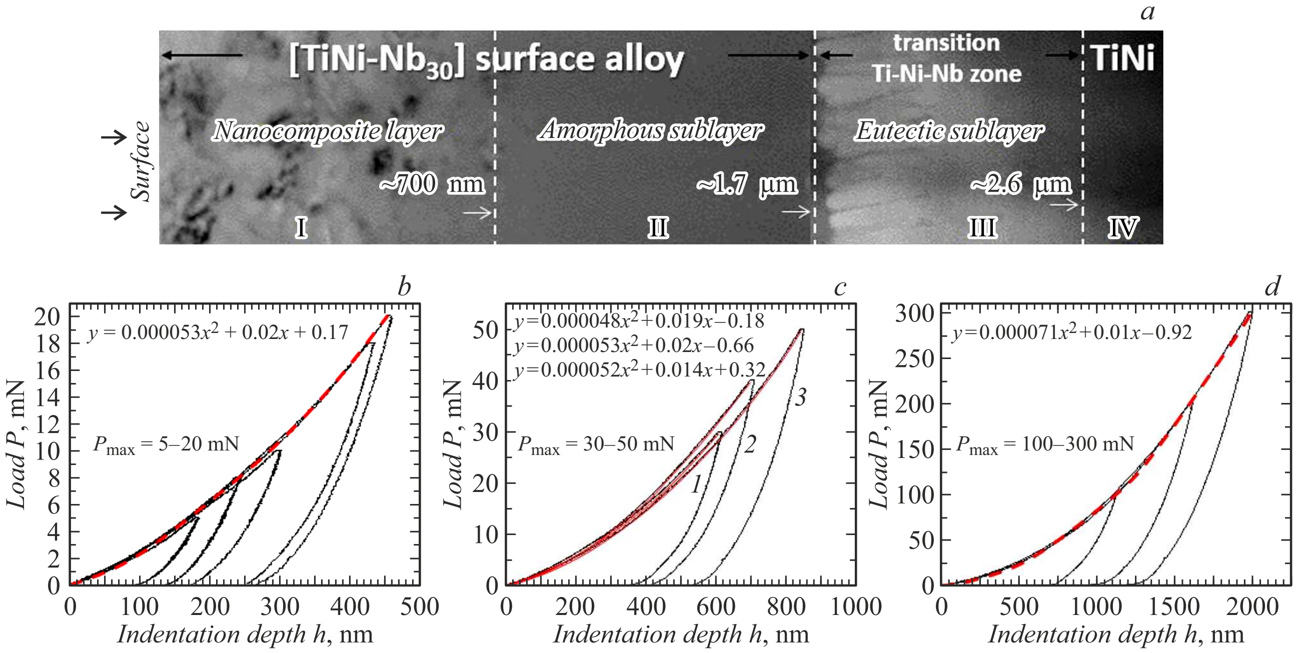

Figure 5. Scheme of the multilayer structure of the [[TiNi$-$Nb$_{30}$]SA/TiNi substrate] system with the indication of the main structural-phase states in the synthesized layers (*a*) and „loading/unloading" diagrams $P-h$ when indenting the system [[TiNi$-$Nb$_{30}$]SA/TiNi substrate] in the loading ranges $P_{\max}$ on the indenter 5$-$20 (*b*), 30$-$50 (*c*) and 100$-$300 mN (*d*).

which are located at a depth from $\sim$ 700 nm to $\sim 2\,\mu$m, the physical and mechanical properties change in a gradient. However, the values of the gradients $dH_{OP}/dh_{\max}$ and $dE_{OP}/dh_{\max}$ in nanocomposite layer I (at a depth of up to $\sim$ 700 nm) are much higher than in sublayers II and III (Fig. 4, curves *1* and *2*). In these sublayers, the strength parameters at a depth from $\sim$ 700 nm to $\sim 2\,\mu$m change as follows. Microhardness H_{OP} and modulus of elasticity E_{OP} decrease linearly from $\sim$ 5 to $\sim$ 3.6 GPa and from $\sim$ 77 to $\sim$ 51 GPa, respectively.

On the contrary, the elastic-plastic parameters in amorphous sublayer II remain at the level $\delta_h \approx 63\%$, $\eta \approx 38\%$, reached at the boundary between layer I and sublayer II (at a depth of $\sim$ 700 nm) to the middle of sublayer II (at a depth of $\sim 1.2\,\mu$m). At a depth from $\sim$ 1.2 to $\sim 2\,\mu$m (to the lower boundary of nanocomposite sublayer III), these parameters change linearly: the plasticity parameter decreases linearly to $\sim$ 59%, the degree of imprint recovery η increases linearly up to $\sim$ 41%. The observed plateau in the dependences of elastic-plastic parameters (at a depth from $\sim$ 700 nm to $\sim 1.2\,\mu$m) and their subsequent linear change (at a depth from $\sim$ 1.2 to $\sim 2\,\mu$m) are due to the structure of amorphous sublayer II with a gradient change in their phase composition and nanoporosity (Fig. 1, *a*). Based on the data on the structure of [TiNi$-$Nb$_{15}$]SA (Fig. 1, *a*), it was found that the values of the elastic-plastic parameters are retained on one level in the region of sublayer II, in which the largest volume fraction of the amorphous phase and the lowest concentration of crystalline nanoparticles of the Ti$_2$Ni phase and nanopores are achieved.

In the eutectic sublayer IV, which represents the transitional Ti$-$Ni$-$Nb-zone from the synthesized [TiNi$-$Nb$_{15}$]SA to the TiNi substrate, the strength and elastic-plastic parameters at a depth of more than $\sim 2\,\mu$m have not changed and have the following values: $H_{OP} \approx 3.6$ GPa, $E_{OP} \approx 51$ GPa, $\delta_h \approx 59\%$, $\eta \approx 41\%$.

Larger symbols in Fig. 4 show the values of the strength and elastic-plastic parameters for the original TiNi sample at a depth of more than $\sim 2\,\mu$m, which are $H_{OP} = 3.5 \pm 0.5$ GPa, $E_{OP} = 55.0 \pm 2.5$ GPa, δ_h=50.0 ± 5.0% and $\eta = 50.0 \pm 5.0\%$. To determine the mechanical compatibility of the synthesized [TiNi$-$Nb$_{15}$]SA layers with the TiNi substrate, it is necessary to compare the obtained values of strength and elastic-plastic parameters for initial TiNi-sample with the values of these parameters for the TiNi-sample with [TiNi$-$Nb$_{15}$]SA at a depth greater than $\sim 2\,\mu$m. It has been established that for a TiNi sample with [TiNi$-$Nb$_{15}$]SA on its surface, the difference in the values of strength and elastic-plastic parameters with the TiNi substrate without irradiation and alloying at a depth of more than $\sim 2\,\mu$m is $\Delta H_{OP} \approx 0.1$ GPa, $\Delta E_{OP} \approx 4$ GPa, $\Delta\delta_h \approx 9\%$, $\Delta\eta \approx 9\%$.

2.2.2. Physical-mechanical properties of the synthesized layers of the system [[TiNi$-$Nb$_{30}$]SA/TiNi-substrate]

Fig. 5 shows the schemes of the layered structure and „loading-unloading" diagrams $P-h$ when indenting the system [[TiNi$-$Nb$_{30}$]SA/TiNi-substrate] in different loading

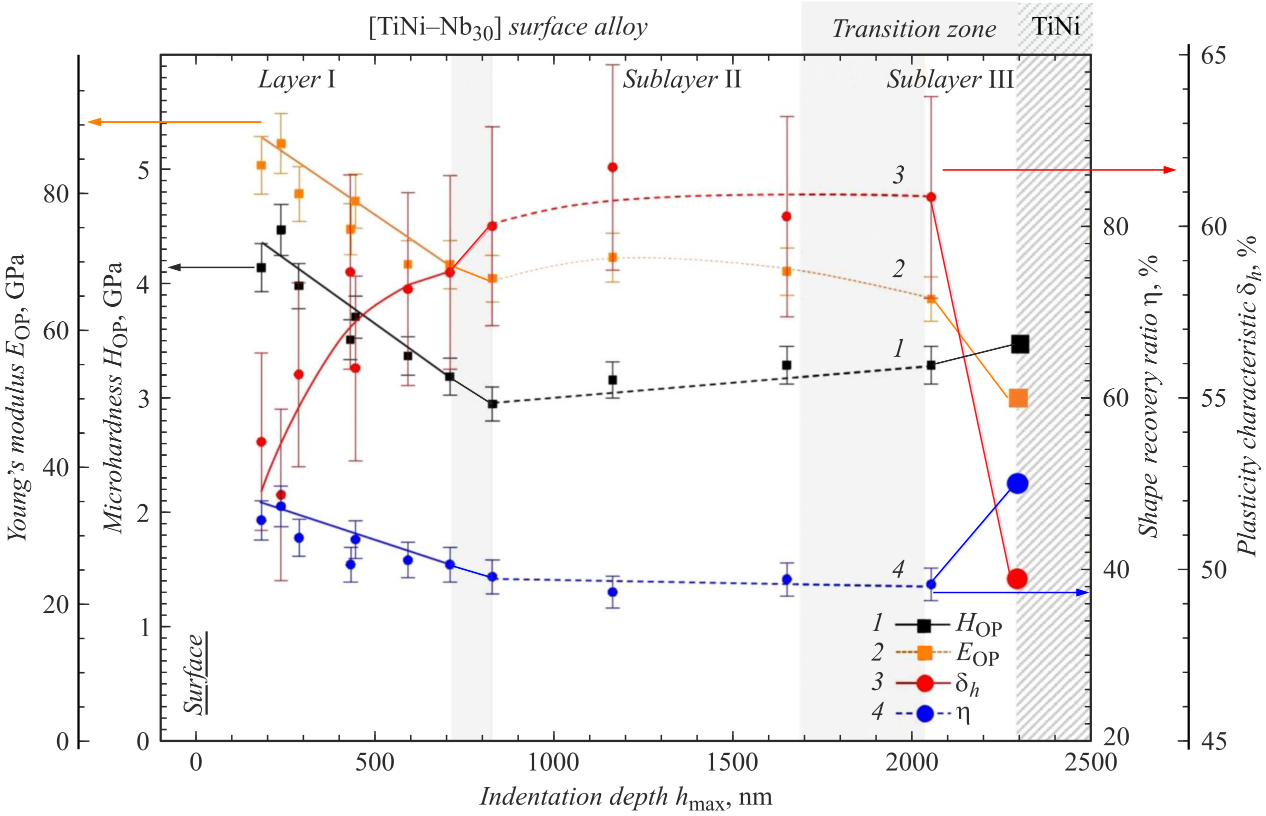

Figure 6. Dependences of microhardness H_{OP} (*1*), elasticity modulus E_{OP} (*2*), plasticity parameter δ_h (*3*) and the shape recovery ratio η (*4*) on the maximum penetration depth of the indenter h_{max} when indenting the system [[TiNi–Nb$_{30}$]SA/TiNi substrate] (larger symbols denote the properties for the initial TiNi sample without irradiation and doping at a depth of more than $\sim 2\,\mu$m).

ranges. As can be seen from Fig. 5, the entire loading range (Fig. 2, *b*) can be divided into three parts:

1) from 5 to 20 mN (Fig. 5, *b*), which corresponds to the maximum immersion depth of the tip h_{max} from ~ 180 to ~ 450 nm;

2) from 30 to 50 mN (Fig. 5, *c*), which corresponds to the immersion depth h_{max} from ~ 600 to ~ 850 nm;

3) from 100 to 300 mN (Fig. 5, *d*), which corresponds to the depth h_{max} from ~ 1.1 to $\sim 2\,\mu$m.

Within the first and third loading ranges, the process of deformation accumulation develops according to a single parabolic dependence with an increase in the load on the indenter. This result is confirmed by the constructed analytical dependences $P(h)$. Inside the second range (depth of immersion h_{max} from ~ 600 to ~ 850 nm), the process of deformation accumulation cannot be described by a single parabolic dependence. This is a consequence of the fact that, at depths from ~ 600 to ~ 850 nm, nanocomposite layer I and sublayer II with a completely amorphous structure are simultaneously involved in the deformation under the indenter tip.

The results of measurements of strength and elastic-plastic parameters characterizing changes in physical and mechanical properties show (Fig. 6) that in nanocomposite layer I at a depth of ~ 180 to ~ 700 nm, the parameter values change in a gradient as follows. Microhardness H_{OP} decreases linearly from ~ 4.5 to ~ 3 GPa, elasticity modulus E_{OP} decreases linearly from ~ 87 to ~ 70 GPa, plasticity parameter δ_h increases monotonically from ~ 53 to $\sim 59\%$, the shape recovery ratio η decreases linearly from ~ 48 to $\sim 41\%$ (Fig. 6, curves *1–4*).

The physical and mechanical properties, as in the case of [TiNi–Nb$_{15}$]SA (Fig. 4), change in a gradient (Fig. 6) with the following features. The strength and elastic-plastic parameters of nanocomposite layer I in [TiNi–Nb$_{30}$]SA are lower, and the gradients of these parameters are smaller than in [TiNi–Nb$_{15}$]SA. From a comparison of the structural and physical and mechanical characteristics of layer I, it follows that the presence of a high volume fraction of the amorphous phase in this layer leads to a decrease in the gradient of physical-mechanical properties compared to [TiNi–Nb$_{15}$]SA.

In sublayer II with a completely amorphous structure, located at a depth from ~ 700 nm to $\sim 1.7\,\mu$m, a plateau is fixed on the dependences of the strength and elastic-plastic parameters, which is characterized by constant values of the parameters $H_{OP} \approx 3.2$ GPa, $E_{OP} \approx 70$ GPa, $\delta_h \approx 60\%$ and $\eta \approx 39\%$. Previously, in a similar way, a plateau on the dependences $\delta_h(h_{max})$ and $\eta(h_{max})$ was found in [TiNi–Nb$_{15}$]SA in amorphous sublayer II (Fig. 4, curves *3* and *4*), where on the upper boundary of this sublayer (at a depth from $\sim 700\,\text{nm}$ to $\sim 1.2\,\mu\text{m}$) in the amorphous matrix, the lowest concentration of crystalline Ti_2Ni nanoparticles and nanopores was observed. On the basis of the presented results, it was possible to establish that an increase in the volume fraction of the amorphous phase leads to an increase in the length of the plateau in the dependences of the strength and elastic-plastic parameters.

In the eutectic sublayer III, which represents the Ti−Ni−Nb transition zone from the synthesized $[\text{TiNi}-\text{Nb}_{30}]$SA to the TiNi substrate, at depths greater than $\sim 2\,\mu\text{m}$ have remained virtually unchanged and are $H_{OP} \approx 3.2\,\text{GPa}$, $E_{OP} \approx 64\,\text{GPa}$, $\delta_h \approx 62\%$ and $\eta \approx 38\%$.

Similarly, in Fig. 6, the larger symbols denote the values of the strength and elastic-plastic parameters for the initial TiNi sample at a depth greater than $\sim 2\,\mu\text{m}$. For a TiNi sample with $[\text{TiNi}-\text{Nb}_{30}]$SA, the difference in strength and elastic-plastic parameters with a TiNi substrate without irradiation and doping at a depth of more than $\sim 2\,\mu\text{m}$ is: $\Delta H_{OP} \approx 0.3\,\text{GPa}$, $\Delta E_{OP} \approx 9\,\text{GPa}$, $\Delta\delta_h \approx 12\%$, $\Delta\eta \approx 12\%$.

The totality of the results indicates that the two-layer $[\text{TiNi}-\text{Nb}_{30}]$SA, which has low strength parameters on the surface ($H_{OP} \approx 4.5\,\text{GPa}$, $E_{OP} \approx 87\,\text{GPa}$) is characterized by lower mechanical compatibility. On the contrary, in $[\text{TiNi}-\text{Nb}_{15}]$SA, which has high strength parameters on the surface ($H_{OP} \approx 9\,\text{GPa}$, $E_{OP} \approx 122\,\text{GPa}$), mechanical compatibility is achieved due to its multilayer structure of SA and the monotonic change in the dependences of the physical and mechanical properties to the TiNi substrate.

Conclusion

Thus, surface Ti−Ni−Nb-alloys, characterized by a multilayer amorphous-nanocomposite structure from a mixture of nanocrystalline, amorphous, and nanocomposite phases, were formed on the surface of a TiNi substrate by the method of additive thin-film electron-beam synthesis. On the basis of quantitative data obtained by instrumented indentation, conclusions are drawn about the relationship between the structure and composition of surface alloys and physical and mechanical properties.

1. Changes in physical and mechanical properties in the synthesized surface Ti−Ni−Nb alloys are due to differences in their layer structure, including the thickness of sublayers, phase compositions, structural states of phases (nanocrystalline and amorphous) in sublayers.

2. High strength and elastic-plastic parameters of the outer layer and a monotonic change in physical and mechanical properties from the surface to the TiNi substrate are provided in the surface Ti−Ni−Nb alloy with a lower volume fraction of the amorphous phase in the synthesized layers.

3. The multilayer structure of the surface Ti−Ni−Nb-alloy and the monotonic change in the physical and mechanical properties of the substrate provide high mechanical compatibility of the synthesized layers to the TiNi substrate.

As a result of the work done, in conclusion, we note an important aspect. The high mechanical compatibility of the synthesized layers with the TiNi substrate, which exhibits inelastic effects, is of practical importance. This property, combined with an amorphous structure with high plasticity, makes it possible to significantly affect the performance of miniature products made of this alloy, to ensure efficient dissipation of energy from mechanical stress concentrators of various nature, localized near the surface at various stages of deformation, and thus to increase the lifetime material before it breaks down.

Acknowledgments

For the organization and assistance in carrying out the work on the synthesis of surface alloys, the authors thank the researchers of the LVE of IHCE SB RAS, Ph.D. A.B. Markov and E.V. Yakovlev.

Funding

The synthesis of surface alloys was carried out by the Government research assignment for ISPMS SB RAS, project FWRW-2021-0003. The study of physical-mechanical properties by instrumented indentation was carried out with the financial support of the Russian Foundation for Basic Research within the framework of the scientific project № 20-33-90034.

Conflict of interest

The authors declare that they have no conflict of interest.

References

[1] J. Zhu, Q. Zeng, T. Fu. Corros. Rev., **37**, 539 (2019). DOI: 10.1515/corrrev-2018-0104

[2] J.J. Mohd, M. Leary, A. Subic, M.A. Gibson. Mater. Des., **56**, 1078 (2014). DOI: 10.1016/j.matdes.2013.11.084

[3] D.F. Williams. Biomaterials, **29**, 2941 (2008). DOI: 10.1016/j.biomaterials.2008.04.023

[4] C.L. Chu, R.M. Wang, T. Hu, L.H. Yin, Y.P. Pu, P.H. Lin, S.L. Wu, C.Y. Chung, K.W.K. Yeung, P.K. Chu. Mater. Sci. Eng., C, **28**, 1430 (2008). DOI: 10.1016/j.msec.2008.03.009

[5] A. Tuissi, S. Carr, J. Butler, A.A. Gandhi, L. O'Donoghue, K. McNamara, J.M. Carlson, S. Lavelle, P. Tiernan, C.A. Biffi, P. Bassani, S.A.M. Tofail. Shap. Mem. Superelasticity, **2**, 196 (2016). DOI: 10.1007/s40830-016-0066-z

[6] *Novel Nanocomposite Coatings. Advances and Industrial Applications*, ed. by R. Daniel, J. Musil (Jenny Stanford Publishing, 2014), 344 p. DOI: 10.1201/b15648

[7] H. Jia, F. Liu, Z. An, W. Li, G Wang, J.P. Chu, J.S.C. Jang, Y. Gao, P.K. Liaw. Thin Solids Films, **561**, 2 (2014). DOI: 10.1016/j.tsf.2013.12.024

[8] E.V. Yakovlev, A.B. Markov, D.A. Shepel, V.I. Petrov, A.A. Neiman. Russ. Phys. J., **63**, 1804 (2021). DOI: 10.1007/s11182-021-02237-1

[9] S.N. Meisner, E.V. Yakovlev, V.O. Semin, L.L. Meisner, V.P. Rotshtein, A.A. Neiman, F. D'yachenko. Appl. Surf. Sci., **437**, 217 (2018). DOI: 10.1016/j.apsusc.2017.12.107

[10] L.L. Meisner, V.P. Rotshtein, V.O. Semin, S.N. Meisner, A.B. Markov, E.V. Yakovlev, F.A. D'yachenko, A.A. Neiman, E.Yu. Gudimova. Surf. Coat. Technol., **404**, 126455 (2020). DOI: 10.1016/j.surfcoat.2020.126455

[11] L.L. Meisner, V.P. Rotshtein, V.O. Semin, A.B. Markov, E.V. Yakovlev, S.N. Meisner, D.A. Shepel, A.A. Neiman, E.Yu. Gudimova, F.A. D'yachenko, R.R. Mukhamedova. Mater. Charact., 166, 110455 (2020). DOI: 10.1016/j.matchar.2020.110455

[12] Y.-L. Zhou, M. Niinomi, T. Akahori, H. Fukui, H. Toda. Mater. Sci. Eng., A, **398**, 28 (2005). DOI: 10.1016/j.msea.2005.03.032

[13] K. Li, Y. Li, X. Huang, D. Gibson, Y. Zheng, J. Liu, L. Sun, Y.-Q. Fu. Appl. Surf. Sci., **414**, 63 (2017). DOI: 10.1016/j.apsusc.2017.04.070

[14] *Medical Coatings and Deposition Technologies*, ed. by D.A. Glocker, S. Ranade (Wiley-Scrivener, 2016), 800 p.

[15] N.H. Marins, C.T.W. Meereis, R.M. Silva, C.P. Ruas, A.S. Takimi, N.L.V. Carreno, F.A. Ogliari. Polym. Bull., **75**, 2301 (2018). DOI: 10.1007/s00289-017-2150-8

[16] G.E. Ozur, D.I. Proskurovsky. Plasma Phys. Rep., **44**, 18 (2018). DOI: 10.1134/S1063780X18010130

[17] W.C. Oliver, G.M. Pharr. J. Mater. Res., **19**, 3 (2004). DOI: 10.1557/jmr.2004.19.1.3

[18] Yu.V. Milman. J. Phys. D: Appl. Phys., **41**, 074013 (2008). DOI: 10.1088/0022-3727/41/7/074013

[19] W. Ni, Y.-T. Cheng, D.S. Grummon. Surf. Coat. Technol., **177-178**, 512 (2004). DOI: 10.1016/S0257-8972Ž03.00920-4

[20] I.E. Permyakova, A.M. Glezer. Perspektivnyye materialy i tekhnologii: monografiya, **1**, 5 (2019) (in Russian) DOI: 10.26201/ISSP.2019.45.557/Adv.mater.V.1.Ch.1

[21] H.W. Zhang, G. Subhash, X.N. Jing, L.J. Kecskes, R.J. Dowding. Philos. Mag. Lett., **86**, 333 (2006). DOI: 10.1080/09500830600788935